

Imaging transverse electron focusing in semiconducting heterostructures with spin-orbit coupling

Andres A. Reynoso, Gonzalo Usaj, and C. A. Balseiro

Instituto Balseiro and Centro Atómico Bariloche,

Comisión Nacional de Energía Atómica, 8400 San Carlos de Bariloche, Argentina.

(Dated: January 30, 2007)

Transverse electron focusing in two-dimensional electron gases (2DEGs) in presence of strong spin-orbit coupling is revisited. The transverse focusing is related basically to the conductance between two contacts at the edge of a 2DEG when a perpendicular magnetic field is applied. Scanning probe microscopy imaging techniques can be used to study the electron flow in these systems. Using numerical techniques we simulate the images that could be obtained with such experiments in systems with strong spin-orbit coupling. We show that hybrid edge states can be imaged and that the outgoing flux can be polarized if the microscope tip probe is placed in specific positions.

I. INTRODUCTION

During the last decade, a tremendous amount of work has been devoted to manipulate and control the spin degree of freedom of the charge carriers.¹ It was promptly recognized that the spin-orbit interaction may be a useful tool to achieve this objective. This is due to the fact that the spin-orbit coupling links currents, spins and external fields. Using intrinsic material properties to control the carrier's spin would allow to build spintronic devices without the complication of integrating different materials in the same circuit.¹ The challenging task of building spin devices based purely on semiconducting technology, requires to inject, control and detect spin polarized currents. During the last years a number of theoretical and experimental papers were devoted to the study of the effect of spin-orbit (SO) coupling on the electronic, magnetic and magnetotransport properties of two dimensional electron gases (2DEG) (see Ref. [2] and references therein). The nature of the SO coupling in these systems is due to the Rashba and the Dresselhaus mechanisms, the latter being the dominant effect in several cases.³ In addition, the Rashba coupling has the advantage that its strength can be changed when a gate voltage is applied to the heterostructure, opening new alternatives for device design.⁴

In many transport experiments in 2DEG with a transverse magnetic field, including quantum Hall effect and transverse magnetic focusing, the SO coupling play a central role. The transverse focusing consists basically in injecting carriers at the edge of a 2DEG and collect them at a distance L from the injection point. The propagation from the injector I to the detector D is ballistic and the carriers can be focalized onto the detector by means of an external magnetic field perpendicular to the 2DEG. The field dependence of the focusing signal is essentially given by the conductance G between the injector I to the detector D that can be calculated using the Landauer approach. In a semiclassical picture, the trajectories that dominate the focusing signal are semicircles whose radius can be tuned with the external field. The new scanning technologies developed in Refs. [5,6] can be used

to map these trajectories. The scanning probe imaging techniques consist on perturbing the system with the tip of a scanning microscope and plot the conductance as a function of the tip position. The conductance change is a map of the electron flow. In this paper we first revisit the theory of transverse electron focusing in systems with strong SO-coupling and interpret the results in terms of a simple semiclassical picture.⁷ Then, we use numerical techniques to simulate the images that could be obtained with scanning probe microscopy experiments in these systems. We show that hybrid edge states can be visualized and that the outgoing flux can be polarized if the microscope tip probe is placed in specific positions

II. TRANSVERSE ELECTRON FOCUSING IN PRESENCE OF STRONG SPIN-ORBIT COUPLING

The Hamiltonian of a 2DEG with Rashba spin-orbit coupling is given by

$$H = \frac{1}{2m^*}(P_x^2 + P_y^2) + \frac{\alpha}{\hbar}(P_y\sigma_x - P_x\sigma_y) - \frac{1}{2}g\mu_B\sigma_z B_z + V(x) \quad (1)$$

here $P_\eta = p_\eta - (e/c)A_\eta$ with p_η and A_η being the η -component of the momentum and vector potential respectively, α is the Rashba coupling parameter, g is the effective g-factor and $\{\sigma_\eta\}$ are the Pauli matrices. $V(x)$ describes the potential at the edge of the sample. In what follows, it is taken as a hard wall potential: $V(x)=0$ for $x \geq 0$ and infinite otherwise. For convenience we choose the vector potential in the Landau gauge $\mathbf{A}=(0, xB_z, 0)$.

Far from the sample edge ($x \gg 0$) the eigenvalues and eigenfunctions of Hamiltonian (1) are well known.⁸ The SO-coupling breaks the spin degeneracy of the Landau levels and the spectrum is given by

$$E_n^\pm = \hbar\omega_c n \mp \sqrt{E_0^2 + \left(\frac{\alpha}{l_c}\right)^2} 2n, \quad (2)$$

where $n \geq 1$, $\omega_c = e|B|/m^*c$ is the cyclotron frequency, $l_c = (\hbar/m\omega_c)^{\frac{1}{2}}$ is the magnetic length, and

$E_0 = \hbar\omega_c/2 - g\mu_B B_z/2$ is the energy of the ground multiplet corresponding to $n = 0$. The eigenfunctions for $n \geq 1$, written as spinors in the z -direction, are⁹

$$\Psi_{n,k}^+(x, y) = \frac{1}{\sqrt{A_n L_y}} e^{iky} \begin{pmatrix} \phi_{n-1}(x - x_0) \\ -D_n \phi_n(x - x_0) \end{pmatrix} \quad (3)$$

and

$$\Psi_{n,k}^-(x, y) = \frac{1}{\sqrt{A_n L_y}} e^{iky} \begin{pmatrix} D_n \phi_{n-1}(x - x_0) \\ \phi_n(x - x_0) \end{pmatrix}, \quad (4)$$

where L_y is the length of the sample in the y -direction, $\phi_n(x - x_0)$ is the harmonic oscillator wavefunction centered at the coordinate $x_0 = l_c^2 k_y$, $A_n = 1 + D_n^2$ and

$$D_n = \frac{\left(\frac{\alpha}{l_c}\right) \sqrt{2n}}{E_0 + \sqrt{E_0^2 + \left(\frac{\alpha}{l_c}\right)^2 2n}}. \quad (5)$$

The wave functions of the first Landau level are given by $\Psi_{n,k}^-(x, y)$ with $n = 0$.

These eigenstates have a cyclotron radius given by

$$r_c^2 = 2 \langle \Psi_n^\pm | (x - x_0)^2 | \Psi_n^\pm \rangle, \quad (6)$$

that for large n gives $r_c^2 \simeq 2n(\hbar/m^*\omega_c)$. We see from Eq.(2) that states with different n , and consequently different cyclotron radius, coexist within the same energy window. Additionally, in the limit of strong Rashba coupling or large n , $D_n \sim 1$ and the spin lies in the plane of the 2DEG always pointing perpendicular to the velocity.

Equivalent results are found in a semiclassical treatment of the problem.^{10,11} In this approach, the spin is described by a vector¹¹ $\mathbf{S} = \hbar/2(n_1(t), n_2(t), n_3(t))$ and the classical orbits are given by

$$\begin{aligned} \mathbf{q} &= r_\pm (\cos \omega_\pm t, \sin \omega_\pm t) \\ \mathbf{S} &= \text{sign}(B_z) \frac{\hbar}{2} (\mp \cos \omega_\pm t, \mp \sin \omega_\pm t, 0), \end{aligned} \quad (7)$$

here \mathbf{q} is the coordinate measured from the centre of the circular orbit of radius

$$r_\pm = \sqrt{\left(\frac{\alpha}{\hbar\omega_c}\right)^2 + \frac{2E}{m^*\omega_c^2}} \pm \frac{\alpha}{\hbar\omega_c}, \quad (8)$$

and the corresponding cyclotron frequencies are

$$\omega_\pm = \text{sign}(B_z)(\omega_c \mp \alpha/\hbar r). \quad (9)$$

In agreement with the quantum results obtained for large n , the spin is found to be in-plane pointing outwards for the smaller orbit and inwards for the bigger one when a positive perpendicular magnetic field B_z is applied. Moreover, the Born-Sommerfeld quantization¹² of these periodic orbits reproduce the exact quantum results of Eq.(2) for large n .

The calculation of the exact edge states with the hard wall potential requires a numerical approach. We have

shown that the semiclassical approximation can be extended to describe edge states in which electrons bounce at the sample edge.¹⁰ Due to the continuity of the wave function and the spin conservation at the edge, the two orbits with radii r_+ and r_- are mixed as schematically shown in figure 1. The agreement between the Born-Sommerfeld quantization of the semiclassical edge states and the quantum results is excellent for states composed of semicircles centered in the edge (normal incidence). In what follows, we use these semiclassical orbits to interpret the numerical results for transverse focusing experiments.

The transverse focusing experiments collect electrons or holes coming from a point contact^{13,14} into another point contact acting as a voltage probe. The carriers are focused onto the collector by the action of an external magnetic field as schematically shown in figure 1. The signal measured in transverse focusing experiments is related to the conductance G between the two point contacts located at a distance L from each other (see figure 1). Typical experimental setups also include two ohmic contacts at the bulk of the 2DEG which are used to inject currents and measure voltages. The details of different configurations with four contacts have been analyzed in Ref. [15]. The main features of the magnetic field dependence of the focusing peaks are contained in the conductance G between the two lateral contacts.¹⁶ Consequently, from hereon we will refer to the focusing signal and to the conductance indistinctly. In the zero temperature limit this conductance is just e^2/h times the transmission coefficient T between the two contacts evaluated at the Fermi energy. For the numerical calculation of T the system was discretized using a tight-binding model in which the leads or contacts are easily attached. In this approach the Hamiltonian is given by $H = H_0 + H_{SO}$ with

$$H_0 = \sum_{n,\sigma} \varepsilon_\sigma c_{n\sigma}^\dagger c_{n\sigma} - \sum_{\langle n,m \rangle, \sigma} t_{nm} c_{n\sigma}^\dagger c_{m\sigma} + h.c.. \quad (10)$$

Here $c_{n\sigma}^\dagger$ creates an electron at site n with spin σ (\uparrow or \downarrow in the z direction) and energy $\varepsilon_\sigma = 4t - \sigma g\mu_B B_z/2$, $t = -\hbar^2/2m^*a_0^2$ and a_0 is the lattice parameter which is always chosen small compared to the Fermi wavelength. The summation is made on a square lattice, the coordinate of site n is $n_x \hat{\mathbf{x}} + n_y \hat{\mathbf{y}}$ where $\hat{\mathbf{x}}$ and $\hat{\mathbf{y}}$ are unit vectors in the x and y directions, respectively. The hard-wall $V(x)$ potential is introduced by taking $n_x > 0$. The hopping matrix element t_{nm} connects nearest neighbors only and includes the effect of the diamagnetic coupling through the Peierls substitution.¹⁷ For the choice of the Landau gauge $t_{n(n+\hat{\mathbf{y}})} = t \exp(in_x 2\pi\phi/\phi_0)$ and $t_{(n+\hat{\mathbf{x}})n} = t$, $\phi = a_0^2 B_z$ is the magnetic flux per plaquette and $\phi_0 = hc/e$ is the flux quantum. The second term of the Hamiltonian describes the spin-orbit coupling,

$$H_{SO} = \sum_n \left\{ \lambda_x c_{n\uparrow}^\dagger c_{(n+\hat{\mathbf{x}})\downarrow} - \lambda_x^* c_{n\downarrow}^\dagger c_{(n+\hat{\mathbf{x}})\uparrow} + e^{in_x 2\pi\phi/\phi_0} \left[\lambda_y c_{n\uparrow}^\dagger c_{(n+\hat{\mathbf{y}})\downarrow} - \lambda_y^* c_{n\downarrow}^\dagger c_{(n+\hat{\mathbf{y}})\uparrow} \right] \right\} + h.c. \quad (11)$$

where $\lambda_x = \alpha/2a_0$ and $\lambda_y = -i\alpha/2a_0$. In what follow we use the following values for the microscopic parameters $a_0 = 5\text{nm}$, $m^* = 0.055m_0$ —here m_0 is the free electron mass—and $E_F = 23\text{meV}$. These parameters correspond to *InAs* based heterostructures with a moderate dop. We use different values of the SO coupling parameter as indicated in each case.

The two lateral contacts, *I* (injector) and *D* (detector) are attached to the semi-infinite 2DEG described by the Hamiltonian (11). Each contact is an ideal (with α narrow stripe of width N_0a_0). They represent point contacts gated to have a single active channel with a conductance $2e^2/h$, for details see ref. [7].

To obtain the conductance between the two contacts we calculate the Green functions between the sites of the injector and the sites of the detector. As the spin is conserved, the Green function between two sites *i* and *j* has four components $\mathcal{G}_{i\sigma,j\sigma'}$. First the propagators of the system without the contacts are obtained by Fourier transforming in the *y*-direction and generating a continuous fraction for each k_y . Having these propagators, the self energies due to the contacts can be easily included using the Dyson equation.¹⁷ The zero temperature conductance is then obtained as

$$G = \frac{e^2}{h} T = \frac{e^2}{h} \text{Tr} \left[\Gamma^{(2)} \mathcal{G}^R \Gamma^{(1)} \mathcal{G}^A \right]_{\omega=E_F} \quad (12)$$

here \mathcal{G}^R and \mathcal{G}^A are the retarded and advanced Green function matrices with elements $\mathcal{G}_{i\sigma,j\sigma'}^R$ and $\mathcal{G}_{i\sigma,j\sigma'}^A$. The matrices $\Gamma^{(l)}$ are given by the self-energy due to contact *l*, $\Gamma^{(l)} = i[\Sigma_l^R - \Sigma_l^A]$ where Σ_l^R and Σ_l^A are the self-energies matrices of the retarded and advanced propagators respectively.

A typical *T* vs. B_z signal for strong spin-orbit coupling is shown in Fig.1(a). A splitting of the first focusing peak is clearly observed.⁷ Notably, there is no splitting of the second peak. These results can be easily interpreted in terms of the semiclassical picture given above. From all the semiclassical orbits that connect the *I* and *D* contacts, the ones that give the largest contribution to the conductance are the ones with $2r_{\pm} = L$.^{7,15} When the applied magnetic field B_z is increased the cyclotron radii are reduced as B_z^{-1} and the first maximum in the transmission is found when $r_-(B_z) = L/2$ as schematically shown in Fig.1.(b). There O_1 is the electron path between the injector *I* and the detector *D*, this path is a semicircle of radius r_- . For this field, indicated as $B_z = B_{1,1}$, the electrons that flow out of the injector in the O_2 orbit do not arrive to the detector since $r_+(B_{1,1}) > L/2$. Furthermore, the two orbits O_1 and O_2 correspond to electrons injected with spin *down* or *up* in the *y*-direction, respectively. Note that due to the SO-coupling, the spin rotates along the orbit. It is convenient to split the total conductance in the four contributions $T_{\alpha\beta}$ corresponding to electrons injected with spin α and collected with spin β . The total transmission can be put as $T = T_{uu} + T_{ud} + T_{du} + T_{dd}$ and for $B_z = B_{1,1}$ the total transmittance is dominated

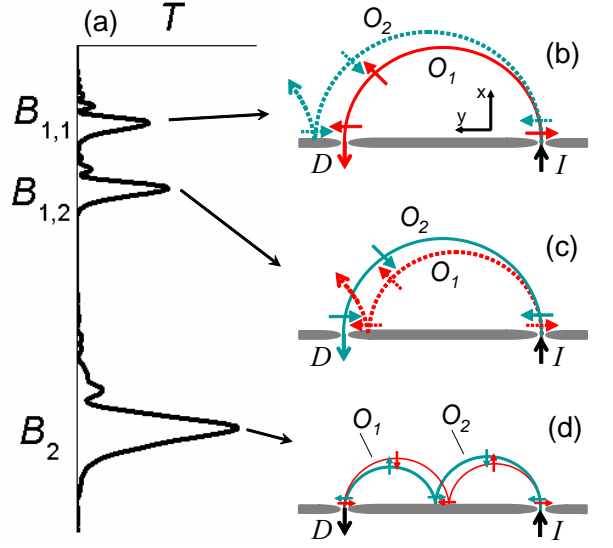


FIG. 1: Panel(a) Transmission coefficient between the contacts *I* and *D* as a function of the applied perpendicular magnetic field in the presence of strong Rashba spin-orbit coupling (qualitative). Relevant semiclassical orbits for three different focusing conditions are shown in panels (b),(c) and (d).

by the contribution T_{du} . When B_z is increased over $B_{1,1}$, $r_-(B_{1,1}) < L/2$ and *T* decreases. The next maximum is reached for $B_z = B_{1,2}$ when $r_+(B_{1,2}) = L/2$ and the relevant orbit is O_2 as shown in Fig.1.(c). For this focusing condition the conductance is dominated by T_{ud} .

The next maximum in *T* is found when $B_z = B_2$ and corresponds to the situation shown in Fig.1.(d). This focusing condition is due to the semiclassical trajectories with one intermediate bounce. In this case the two possible paths O_1 and O_2 contribute to the conductance. Electrons leaving the injector *I* with a given spin arrive at the detector *D* with the same spin projection. Accordingly, the total coefficient *T* is dominated by $T_{uu} + T_{dd}$. Clearly, B_2 is the magnetic field for which $2(r_- + r_+) = L$ holds. Extrapolating the semiclassical picture shown in the figure one finds that the odd peaks (sorted by ascending magnetic field) split while the even peaks remain unsplit in agreement with the exact numerical result.

III. IMAGING TECHNIQUES IN TRANSVERSE FOCUSING WITH SPIN-ORBIT COUPLING

Scanning probe microscopy (SPM) techniques have been recently used for imaging the electron flow in a variety of 2DEG ballistic systems.^{5,6} With this technique, the negatively charged tip of a scanning microscope is positioned above the 2DEG as schematically shown in Fig.2(c). The tip position can be changed to swept a given area of the explored 2D device. The electrons under the tip are repelled and consequently a zone of lower

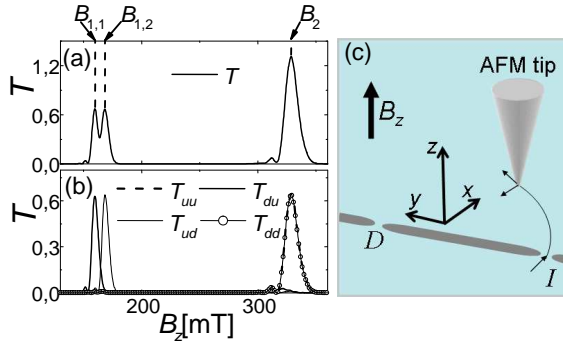


FIG. 2: (a) Total focusing transmission coefficient T vs applied perpendicular magnetic field B_z . (b) Spin-resolved transmission coefficients versus B_z . We used $E_F = 23$ meV, $m^* = 0.055m_0$, $\alpha = 7$ meVnm, $\beta = 0$, $L = 1.5 \mu\text{m}$ and the width of the contacts is 70nm . (c) Schematic of an SPM imaging procedure.

electron density (or *divot*) is formed under the tip. In the simplest case the conductance between two contacts of the device is measured as the tip position changes; if the tip is located in a region that affects the electron flow between the contacts the conductance changes, providing a map of the electron flow in the device. The resolution of these images is lower than the divot size,^{5,6} making this technique a powerful tool for studying nano-scale ballistic systems.

Here, we propose the use of this technique to explore the transverse focusing in the presence of spin-orbit interaction.¹⁸ We simulate the effect of the tip potential by perturbing (increasing) the energies $\varepsilon_{i,\sigma}$ of the sites i in an area of the order of 100nm^2 centered at the tip position. The Dyson equation is used to introduce the perturbation and the exact propagators between the contacts I and D are calculated for each position of the tip.

Figure 3 panel (a) shows the conductance vs the tip position when the perpendicular magnetic field is fixed to obtain the first maximum of conductance ($B_z = B_{1,1}$) for a SO-coupling $\alpha = 7$ meVnm. The semicircular electron path is clearly observed. In this case the conductance map is dominated by a drop in the conductance along the O_1 path. A similar pattern is found for the second conductance maximum ($B_z = B_{1,2}$) as shown in Fig. 3(b). In this case, the conductance drop is due to the scattering induced by the tip of electrons traveling along the O_2 path. A slightly different situation is found when B_z is fixed in between $B_{1,1}$ and $B_{1,2}$ as shown in panel (c) of the same figure; although the conductance variation is also dominated by a drop (dark area), the conductance increases at the two sides of the minimum. The observation of these two lobes shows that the tip, when placed at those positions, modifies the electron flow making a non-focalized electron path— O_1 or O_2 in Fig.1(b)-(c)—to contribute to the conductance.

More interesting are the imaging results obtained when

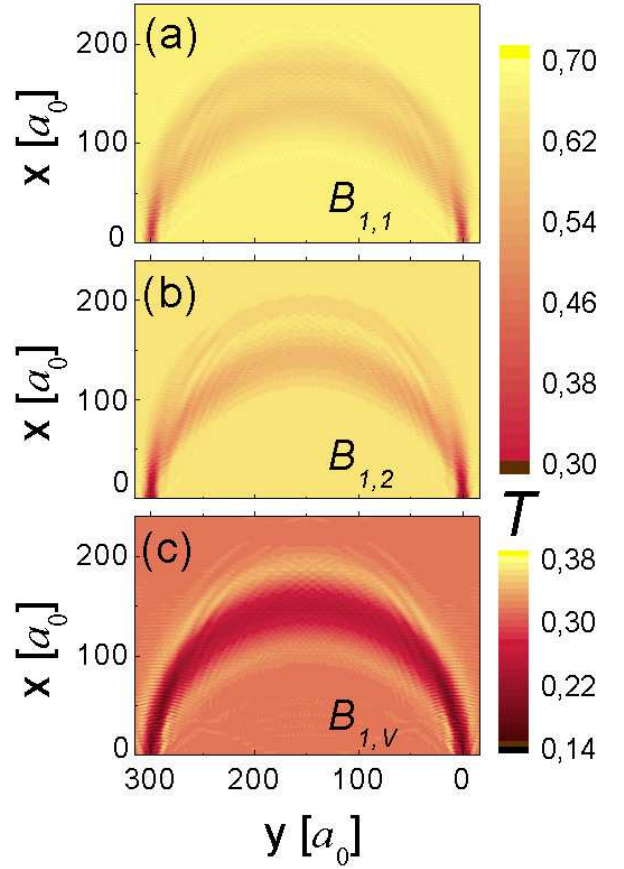


FIG. 3: Total transmission coefficient (conductance) between the contacts 1 and 2 as a function of the probe position for (a) $B_z = B_{1,1}$, (b) $B_z = B_{1,2}$ and (c) $B_z = B_{1,v} = (B_{1,1} + B_{1,2})/2$. We used $\alpha = 7$ meVnm and the parameters given in Fig.2.

the field is fixed at the second focusing condition: $B_z = B_2$. As shown above, in this case the conductance is dominated by the electron orbits with one bounce at the sample's edge. For this field the largest contributions to the transmission coefficient are T_{uu} and T_{dd} , and the corresponding focusing peak is unsplit. In Fig.4 and Fig.5 the results for this case are shown for $\alpha = 7$ meVnm and 15 meVnm, respectively. Panel (a) shows T_{uu} as a function of the position of the microscope probe. The change in the conductance in this case clearly shows that the electrons injected with spin *up* (in the y -direction) leave the injector in the bigger orbit, rebound and then arrive to the detector in the smaller orbit with spin *up*—see O_2 in Fig.1(d). In panel (b) the transmittance T_{dd} is shown—see O_1 in Fig.1(d)—and in panel (c) the total transmission coefficient is presented. As T_{ud} and T_{du} are very small, the total transmission is essentially given by the sum of the contributions shown in panels (a) and (b). Experimentally these two contributions could be distinguished by selecting the spin of the injected carriers. In fact a combination of an external in-plane magnetic field in the y -direction and an appropriate gate voltage in the

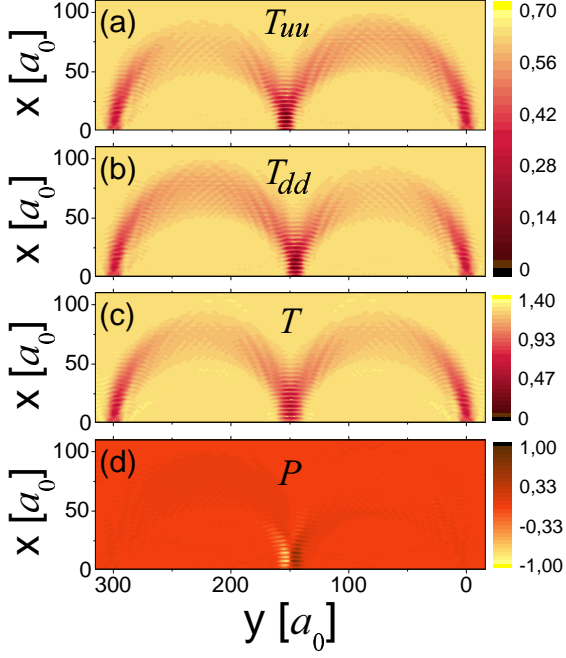


FIG. 4: We plot (a) T_{uu} , (b) T_{dd} , (c) T and (d) P as a function of the probe position for $B_z = B_2$. We used $\alpha = 7\text{meVnm}$ and the parameters given in Fig.2.

point contacts can be used to filter spins in the injector or detector¹³. Selecting the spin of the injected electrons would enable to separate the two trajectories—(a) and (b) in figures 4 and 5—and obtain a direct visualization of the two orbits split by the spin-orbit coupling. Conversely, selecting the spin of the detector point contact, the transmissions $T_+ = T_{uu} + T_{du}$ and $T_- = T_{ud} + T_{dd}$ of carriers arriving at D with spin *up* and *down*, respectively, could be measured. In terms of these quantities, we define the polarization P of the transmitted particles as

$$P = \frac{T_+ - T_-}{T}$$

Panel (c) and (d) of figures 4 and 5 show the total transmission coefficient T and the polarization P as a function of the tip position. The two semicircular electron paths including the rebound at the edge are visualized in the conductance map. In our simulations the smaller and the bigger electron paths are not easily resolved in total transmission coefficient map except for the largest SO-coupling case and for the tip close to the bounce position—see Fig.5(c). There, an appreciable fall (about 50%) of the conductance in the two rebound positions suggests that, when the probe is positioned there, the contribution to the transmission of one of the two possible electron paths (O_1 or O_2) is being suppressed. If O_1 is being suppressed, the electrons arriving to the detector will have spin *up*. On the other hand, if O_2 is

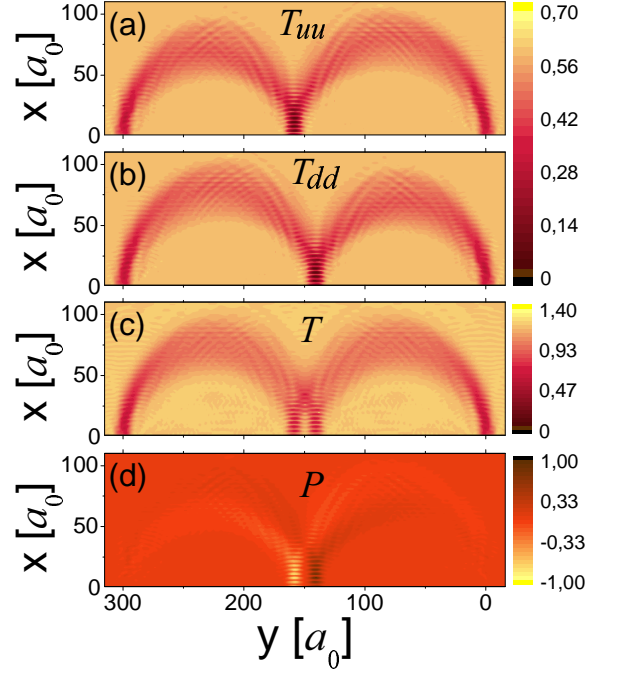


FIG. 5: We plot (a) T_{uu} , (b) T_{dd} , (c) T and (d) P as a function of the probe position for $B_z = B_2$. We used $\alpha = 15\text{meVnm}$ and the parameters given in Fig.2.

suppressed only spin *down* electrons arrive to the detector. This means that one can select the spin polarization of the outgoing carrier flux by changing the tip position a few nanometers as shown in Fig.4(d) and Fig.5(d). Notably, the effect is also clearly observed in the case of the smaller SO-coupling despite of the fact that the total transmittance T does not resolve the two orbits.

IV. SUMMARY AND CONCLUSIONS

We have studied scanning probe microscopy imaging techniques for the case transverse electron focusing in two-dimensional electron gases (2DEGs) with strong Rashba coupling. The main results can be summarized as follows:

- i.- The existence of two different cyclotron radii splits the first focusing peak onto two sub-peaks, each one corresponds to electrons arriving to the detector with different spin polarizations along the direction parallel to the sample's edge.
- ii.- The images of the electron flow for focusing fields corresponding to the first two sub-peaks are very similar and consequently, for this case, the technique can not clearly distinguish the two type of orbits.
- iii.- When the field is fixed between the focusing fields of the two sub-peaks, $B_z = (B_{1,1} + B_{1,2})/2$, the conductance map shows a structure that suggests the existence

of the two orbits.

iv.- For the second focusing condition, and for the case of strong Rashba coupling, the technique can resolve the two orbits when the microscope tip is placed close to the rebound coordinate.

v.- For the case described in the previous point, the microscope tip can be used to polarize the electron flux arriving at the detector. The direction of the polarization can be reversed by changing the tip position a few nanometers.

Some final comments are:

vi.- Interference fringes - characteristic of the quantum ballistic transport regime are observed in all the conductance maps.

vii.- In different configurations with strong Rashba coupling, replacing the hard wall potential $V(x)$ by a more realistic parabolic potential does not change main properties of the system.^{19,20} Based on these results, we

do not expect quantitative changes in the obtained images if the model $V(x)$ is replaced by a realistic confining potential for heterostructures defined by gates.

viii.- We have analyzed in detail the competition between Rashba and Dresselhaus coupling.²¹ The main effect of such a competition is the well known partial cancellation of the spin-orbit effects^{3,22} and the rotation of the spin along new directions that depend on the relative strength of the two SO couplings.

V. ACKNOWLEDGMENT

This work was supported by ANPCyT Grants No 13829 and 13476 and CONICET PIP 5254. AR and GU acknowledge support from CONICET. AR acknowledge support from PITP.

-
- ¹ D. Awschalom, N. Samarth, and D. Loss, eds., *Semiconductor Spintronics and Quantum Computation* (Springer, New York, 2002).
 - ² A. Reynoso, G. Usaj, and C. A. Balseiro, Phys. Rev. B **73**, 115342 (2006).
 - ³ R. Winkler, *Spin-orbit coupling effects in two-dimensional electron and hole systems* (Springer-Verlag, 2003).
 - ⁴ J. Nitta, T. Akazaki, H. Takayanagi, and T. Enoki, Phys. Rev. Lett. **78**, 1335 (1997).
 - ⁵ M. Topinka, B. LeRoy, S. Shaw, E. Heller, R. Westervelt, K. Maranowski, and A. Gossard, Science (2000).
 - ⁶ M. Topinka, B. LeRoy, R. Westervelt, S. Shaw, R. Fleischmann, E. Heller, K. Maranowski, and A. Gossard, Nature **410**, 183 (2001).
 - ⁷ G. Usaj and C. A. Balseiro, Phys. Rev. B **70**, 041301(R) (2004).
 - ⁸ Y. A. Bychkov and E. I. Rashba, JETP Letters **39**, 78 (1984).
 - ⁹ These are the solutions for positive B_z . For negative B_z the eigenstates change: $\Psi_{n,k}^{\pm}|_{-|B_z|} = i\sigma_y \Psi_{n,k}^{\pm}|_{|B_z|}$.
 - ¹⁰ A. Reynoso, G. Usaj, M. J. Sanchez, and C. A. Balseiro, Phys. Rev. B **70**, 235344 (2004).
 - ¹¹ M. Pletyukhov, C. Amann, M. Mehta, and M. Brack, Phys. Rev. Lett. **89**, 116601 (2002).
 - ¹² M. Gutzwiller, *Chaos in Classical and Quantum Mechanics* (Spring-Verlag, New York, 1991).
 - ¹³ R. M. Potok, J. A. Folk, C. M. Marcus, and V. Umansky, Phys. Rev. Lett. **89**, 266602 (2002).
 - ¹⁴ L. P. Rokhinson, V. Larkina, Y. B. Lyanda-Geller, L. N. Pfeiffer, and K. W. West, Phys. Rev. Lett. **93**, 146601 (2004).
 - ¹⁵ H. van Houten, C. W. J. Beenakker, J. G. Williamson, M. E. I. Broekaart, P. H. M. Loosdrecht, B. J. van Wees, J. E. Mooji, C. T. Foxon, and J. J. Harris, Phys. Rev. B **39**, 8556 (1989).
 - ¹⁶ C. W. Beenakker and H. van Houten, in *Solid State Physics*, edited by H. Ehrenreich and D. Turnbull (Academic Press, Boston, 1991), vol. 44, pp. 1–228.
 - ¹⁷ D. K. Ferry and S. M. Goodnick, *Transport in Nanostructures* (Cambridge University Press, New York, 1997).
 - ¹⁸ Imaging of cyclotron orbits using this imaging technique was reported at ICPS 28, Vienna (2006) by K. Aidala. See also Ref. [23].
 - ¹⁹ G. Usaj and C. A. Balseiro, Europhys. Lett. **72**, 631 (2005).
 - ²⁰ A. O. Govorov, A. V. Kalameitsev, and J. P. Dulka, Phys. Rev. B **70**, 245310 (2004).
 - ²¹ A. Reynoso, G. Usaj, C. A. Balseiro, to be published.
 - ²² J. Schliemann and D. Loss, Phys. Rev. B **68**, 165311 (2003).
 - ²³ K. E. Aidala, R. E. Parrott, E. Heller, and R. Westervelt (2006), cond-mat/0603035.